J. Korean Soc. Ind. Appl. Math. Vol.27, No.2, 109–122, 2023 https://doi.org/10.12941/jksiam.2023.27.109

APPLICATION OF THE BIFOCUSING METHOD IN MICROWAVE IMAGING WITHOUT BACKGROUND INFORMATION

SEONG-HO SON[1] AND WON-KWANG PARK[2,†]

[1]DEPARTMENT OF MECHANICAL ENGINEERING, SOONCHUNHYANG UNIVERSITY, ASAN, 31538, KOREA
Email address: son@sch.ac.kr

[2]DEPARTMENT OF INFORMATION SECURITY, CRYPTOLOGY, AND MATHEMATICS, KOOKMIN UNIVERSITY, SEOUL, 02707, KOREA
Email address: [†]parkwk@kookmin.ac.kr

ABSTRACT. In this study, we consider the application of the bifocusing method (BFM) for identifying the locations and shapes of small anomalies from scattering parameter data when the exact values of background permittivity and conductivity are unknown. To this end, an imaging function using numerical focusing operator is introduced and its mathematical structure is revealed by establishing a relationship with an infinite series of Bessel functions, antenna arrangements, and anomaly properties. On the basis of the revealed structure, we demonstrate why inaccurate location and size of anomalies were retrieved via the BFM. Some simulation results are illustrated using synthetic data polluted by random noise to support the theoretical result.

1. INTRODUCTION

Retrieving the location, outline shape, and material properties (or parameter distribution) of unknown targets is an interesting and important research subject for addressing inverse scattering problems and microwave imaging inadequacies. To this end, various qualitative methods using multistatic measurement systems have been investigated. For example, direct sampling method [1, 2, 3], factorization method [4, 5, 6], Kirchhoff and subspace migration techniques [7, 8, 9], linear sampling method [10, 11, 12], MUltiple SIgnal Classification (MUSIC) algorithm [13, 14, 15], orthogonality sampling method [16, 17, 18], and topological derivative [19, 20, 21]. We also refer to [22, 23, 24, 25, 26, 27, 28] for related research.

The recently developed bifocusing method (BFM) is also classified as a qualitative method using a multistatic measurement system. Based on applications for ultra-wide-band tomographic radar imaging [29], damage detection in concrete voids [30], and anomaly detection

Received May 8 2023; Revised June 19 2023; Accepted in revised form June 20 2023; Published online June 25 2023.

2000 *Mathematics Subject Classification.* 78A46.

Key words and phrases. Bifocusing Method, Scattering Parameter, Microwave Imaging, Background Information.

[†] Corresponding author.

in microwave imaging [31], the BFM can be considered an effective microwave imaging technique. To perform the BFM to retrieve unknown targets, the incident field at each search point must be evaluated with the exact value of the background wavenumber, which is dependent to applied frequency, background permittivity, permeability, and conductivity; therefore, exact information regarding the background medium must be known. For this reason, most research has assumed that complete information is known regarding the background and used the statistical values.

Notably, if inaccurate values for background permittivity or conductivity are applied, the BFM is inappropriate for reconstructing unknown targets, as inaccurate locations and target sizes are identified. Fortunately, it is possible to recognize the targets when the value of applied background conductivity is small; however this approach has been heuristically examined using numerical simulations. To the best of our knowledge, mathematical theory for explaining this phenomenon has not been established yet. This motivates our investigation to develop a mathematical theory for applying the BFM.

In this study, we establish a reliable mathematical theory of the BFM from scattering parameter data without complete background medium information. To do so, we apply an alternative wavenumber rather than the true and demonstrate that the imaging function of the BFM can be expressed using the infinite series of Bessel functions of integer order, material properties, antenna arrangement, and true and applied wavenumbers. This is based on the integral representation formula for the scattered-field $S-$parameter in the presence of small anomalies. The results reveal the reason that inaccurate locations and target shapes are retrieved. Simulation is conducted using synthetic data generated by the CST STUDIO SUITE to validate the theoretical results.

This paper is organized as follows. In Section 2, we briefly introduce the concept of the scattered-field $S-$parameter in the presence of small anomalies and the imaging function of the BFM. In Section 3, we develop the mathematical structure of the designed imaging function by establishing a relationship with an infinite series of Bessel functions of integer order, antenna arrangement, material properties, and unknown background information. Based on this structure, we explain the reason that inaccurate locations and shapes are retrieved. In Section 4, simulation results using synthetic data that are polluted by random noise are presented to support our theoretical results. A brief conclusion including future research directions is provided in Section 5.

2. Scattering Parameter and Bifocusing Method

2.1. **Problem Setting.** Suppose that there exists a set of anomalies (Σ_s, $s = 1, 2, \cdots, S$) that have ε_s and σ_s as the value of dielectric permittivity and electric conductivity at given angular frequency $\omega = 2\pi f$, respectively. For the sake of experimentation, we assume that every Σ_s is a small ball with radii α_s, and denote Σ be the collection of Σ_s. Throughout this study, we set every Σ_s to be completely embedded in a homogeneous region Ω and there no magnetic material is present in Ω; thus, the value of magnetic permeability is constant $\mu(\mathbf{r}) \equiv \mu_{\mathrm{b}} = 4\pi \times 10^{-7}\,\mathrm{H/m}$ for every $\mathbf{r} \in \Omega$. We set Ω to be filled by a matching liquid, which

has $\varepsilon_{\rm b}$ and $\sigma_{\rm b}$ as the value of permittivity and conductivity at ω such that $\omega\varepsilon_{\rm b} \gg \sigma_{\rm b}$. Using this notation, we introduce the piecewise constant permittivity and conductivity as follows:

$$\varepsilon(\mathbf{r}) = \begin{cases} \varepsilon_s & \text{for} \quad \mathbf{r} \in \Sigma_s \\ \varepsilon_{\rm b} & \text{for} \quad \mathbf{r} \in \Omega\backslash\overline{\Sigma} \end{cases} \quad \text{and} \quad \sigma(\mathbf{r}) = \begin{cases} \sigma_s & \text{for} \quad \mathbf{r} \in \Sigma_s \\ \sigma_{\rm b} & \text{for} \quad \mathbf{r} \in \Omega\backslash\overline{\Sigma}. \end{cases}$$

We denote $k = \omega\sqrt{\mu_{\rm b}(\varepsilon_{\rm b} + i\sigma_{\rm b}/\omega)}$ as the background wavenumber and $\mathbf{A}_n$, $n = 1, 2, \cdots, N$ as the dipole antenna with location $\mathbf{a}_n$ for transmitting and receiving signals. With this setting, we assume that all anomalies Σ_s are separated from each other such that:

$$|\mathbf{r}' - \mathbf{r}''| \gg \frac{1}{4|k|} \quad \text{for} \quad \mathbf{r}' \in \Sigma_{s'}, \quad \mathbf{r}'' \in \Sigma_{s''}, \quad s' \neq s'', \quad s', s'' = 1, 2, \cdots, S. \tag{2.1}$$

We also assume that $\mathbf{a}_n$ and $\mathbf{r}' \in \Sigma$ satisfy the relation (2.1), and to guarantee the smallness of Σ_s, the following relation holds (e.g., see [32]):

$$\sqrt{\frac{\varepsilon_s}{\varepsilon_{\rm b}}} - 1 < \frac{\lambda}{4\alpha_s}, \quad s = 1, 2, \cdots, S, \tag{2.2}$$

where λ denotes the positive wavelength. We illustrate the problem setting in Fig. 1.

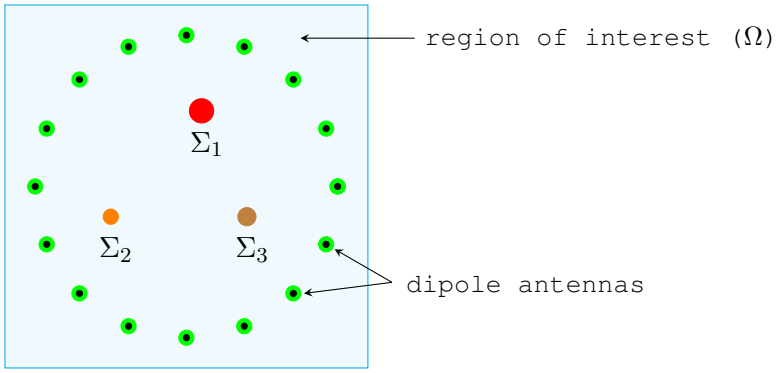

FIGURE 1. Illustration of problem setting.

2.2. **Scattering Parameter.** Let $\mathbf{E}_{\rm inc}(\mathbf{a}_m, \mathbf{r})$ be the incident field due to the point current density $\mathbf{J}$ at $\mathbf{A}_m$. Then, based on Maxwell's equation, $\mathbf{E}_{\rm inc}(\mathbf{a}_m, \mathbf{r})$ satisfies the following:

$$\nabla \times \mathbf{E}_{\rm inc}(\mathbf{a}_m, \mathbf{r}) = -i\omega\mu_{\rm b}\mathbf{H}_{\rm inc}(\mathbf{a}_m, \mathbf{r}), \quad \nabla \times \mathbf{H}_{\rm inc}(\mathbf{a}_m, \mathbf{r}) = (\sigma_{\rm b} + i\omega\varepsilon_{\rm b})\mathbf{E}_{\rm inc}(\mathbf{a}_m, \mathbf{r}).$$

We denote $\mathbf{E}_{\rm tot}(\mathbf{r}, \mathbf{a}_m)$ as the corresponding total field in the presence of Σ measured by the receiver $\mathbf{A}_m$, which satisfies the following:

$$\nabla \times \mathbf{E}_{\rm tot}(\mathbf{r}, \mathbf{a}_m) = -i\omega\mu_{\rm b}\mathbf{H}_{\rm tot}(\mathbf{r}, \mathbf{a}_m), \quad \nabla \times \mathbf{H}_{\rm tot}(\mathbf{r}, \mathbf{a}_m) = (\sigma(\mathbf{r}) + i\omega\varepsilon(\mathbf{r}))\mathbf{E}_{\rm tot}(\mathbf{r}, \mathbf{a}_m)$$

with transmission condition on $\partial\Sigma$. Here, $\mathbf{H}_{\rm inc}$ and $\mathbf{H}_{\rm tot}$ denote the magnetic fields.

The $S-$parameter (or scattering parameter) is defined as the ratio of the output voltages (or reflected waves) at the $\mathbf{A}_n$ to the input voltages (or incident waves) at $\mathbf{A}_m$, referencing

[33]. We denote $S_{\rm inc}(n,m)$ and $S_{\rm tot}(n,m)$ as the incident and total field $S-$parameter with and without anomalies. Throughout this study, the measurement data $S_{\rm scat}(n,m)$ denotes the scattered field $S-$parameter obtained by subtracting $S_{\rm tot}(n,m)$ and $S_{\rm inc}(n,m)$. Referencing [34], $S_{\rm scat}(n,m)$ can be represented by the following integral equation:

$$S_{\rm scat}(n,m)=\frac{ik^2}{4\omega\mu_{\rm b}}\int_{\Omega}\left(\frac{\varepsilon(\mathbf{r}')-\varepsilon_{\rm b}}{\varepsilon_{\rm b}}+i\frac{\sigma(\mathbf{r}')-\sigma_{\rm b}}{\omega\varepsilon_{\rm b}}\right)\mathbf{E}_{\rm inc}(\mathbf{a}_m,\mathbf{r}')\cdot\mathbf{E}_{\rm tot}(\mathbf{r}',\mathbf{a}_n){\rm d}\mathbf{r}'.$$

In this study, the height of microwave machine is considered to be long enough (see [35] for an example of the experimental setup). Therefore, based on the mathematical treatment of the scattering of time-harmonic electromagnetic waves from thin infinitely long cylindrical obstacles, only the $z-$component of the incident and total fields can be measured, and by denoting $\mathrm{E}^{(z)}_{\rm inc}$ and $\mathrm{E}^{(z)}_{\rm tot}$ as the $z-$component of the incident and total fields, respectively, the expression $S_{\rm scat}(n,m)$ becomes the following:

$$S_{\rm scat}(n,m)=\frac{ik^2}{4\omega\mu_{\rm b}}\int_{\Sigma}\left(\frac{\varepsilon(\mathbf{r}')-\varepsilon_{\rm b}}{\varepsilon_{\rm b}}+i\frac{\sigma(\mathbf{r}')-\sigma_{\rm b}}{\omega\varepsilon_{\rm b}}\right)\mathrm{E}^{(z)}_{\rm inc}(\mathbf{a}_m,\mathbf{r}')\mathrm{E}^{(z)}_{\rm tot}(\mathbf{r}',\mathbf{a}_n){\rm d}\mathbf{r}'. \quad (2.3)$$

2.3. **Bifocusing Method: Traditional Approach.** We next introduce the imaging function of the BFM to retrieve Σ_s from the scattering matrix $\mathbb{M}$ in which the elements are measurement data $S_{\rm scat}(n,m)$, which are determined as follows:

$$\mathbb{M}=\begin{pmatrix} S_{\rm scat}(1,1) & S_{\rm scat}(1,2) & \cdots & S_{\rm scat}(1,N-1) & S_{\rm scat}(1,N)\\ S_{\rm scat}(2,1) & S_{\rm scat}(2,2) & \cdots & S_{\rm scat}(2,N-1) & S_{\rm scat}(2,N)\\ \vdots & \vdots & \ddots & \vdots & \vdots\\ S_{\rm scat}(N,1) & S_{\rm scat}(N,2) & \cdots & S_{\rm scat}(N,N-1) & S_{\rm scat}(N,N)\end{pmatrix}$$

Unfortunately, since the complete expression of the total field $\mathrm{E}^{(z)}_{\rm tot}(\mathbf{r},\mathbf{a}_n)$ is still unknown, an alternative expression of $S_{\rm scat}(n,m)$ is required. Since (2.2) holds, by applying the Born approximation to (2.3), we have

$$S_{\rm scat}(n,m)\approx\frac{ik^2}{4\omega\mu_{\rm b}}\int_{\Sigma}\left(\frac{\varepsilon(\mathbf{r}')-\varepsilon_{\rm b}}{\varepsilon_{\rm b}}+i\frac{\sigma(\mathbf{r}')-\sigma_{\rm b}}{\omega\varepsilon_{\rm b}}\right)\mathrm{E}^{(z)}_{\rm inc}(\mathbf{a}_m,\mathbf{r}')\mathrm{E}^{(z)}_{\rm inc}(\mathbf{r}',\mathbf{a}_n){\rm d}\mathbf{r}'. \quad (2.4)$$

Correspondingly, $\mathbb{M}$ can be represented as follows:

$$\mathbb{M}\approx\frac{ik^2}{4\omega\mu_{\rm b}}\begin{pmatrix} \displaystyle\int_{\Sigma}\mathcal{O}(\mathbf{r}')\mathrm{E}^{(z)}_{\rm inc}(\mathbf{a}_1,\mathbf{r}')\mathrm{E}^{(z)}_{\rm inc}(\mathbf{a}_1,\mathbf{r}'){\rm d}\mathbf{r}' & \cdots & \displaystyle\int_{\Sigma}\mathcal{O}(\mathbf{r}')\mathrm{E}^{(z)}_{\rm inc}(\mathbf{a}_1,\mathbf{r}')\mathrm{E}^{(z)}_{\rm inc}(\mathbf{a}_N,\mathbf{r}'){\rm d}\mathbf{r}'\\ \displaystyle\int_{\Sigma}\mathcal{O}(\mathbf{r}')\mathrm{E}^{(z)}_{\rm inc}(\mathbf{a}_2,\mathbf{r}')\mathrm{E}^{(z)}_{\rm inc}(\mathbf{a}_1,\mathbf{r}'){\rm d}\mathbf{r}' & \cdots & \displaystyle\int_{\Sigma}\mathcal{O}(\mathbf{r}')\mathrm{E}^{(z)}_{\rm inc}(\mathbf{a}_2,\mathbf{r}')\mathrm{E}^{(z)}_{\rm inc}(\mathbf{a}_N,\mathbf{r}'){\rm d}\mathbf{r}'\\ \vdots & \ddots & \vdots\\ \displaystyle\int_{\Sigma}\mathcal{O}(\mathbf{r}')\mathrm{E}^{(z)}_{\rm inc}(\mathbf{a}_N,\mathbf{r}')\mathrm{E}^{(z)}_{\rm inc}(\mathbf{a}_N,\mathbf{r}'){\rm d}\mathbf{r}' & \cdots & \displaystyle\int_{\Sigma}\mathcal{O}(\mathbf{r}')\mathrm{E}^{(z)}_{\rm inc}(\mathbf{a}_N,\mathbf{r}')\mathrm{E}^{(z)}_{\rm inc}(\mathbf{a}_N,\mathbf{r}'){\rm d}\mathbf{r}'\end{pmatrix}, \quad (2.5)$$

where

$$\mathcal{O}(\mathbf{r}') = \frac{\varepsilon(\mathbf{r}') - \varepsilon_{\rm b}}{\varepsilon_{\rm b}} + i\frac{\sigma(\mathbf{r}') - \sigma_{\rm b}}{\omega\varepsilon_{\rm b}}.$$

On the basis of (2.5), we next design the imaging function by synthesizing two focused groups of antennas. To this end, we define the following vector: for each $\mathbf{r} \in \Omega$,

$$\mathbf{W}(\mathbf{r}) = \left(\frac{1}{\mathrm{E}^{(z)}_{\rm inc}(\mathbf{a}_1, \mathbf{r})}, \frac{1}{\mathrm{E}^{(z)}_{\rm inc}(\mathbf{a}_2, \mathbf{r})}, \cdots, \frac{1}{\mathrm{E}^{(z)}_{\rm inc}(\mathbf{a}_N, \mathbf{r})} \right) \tag{2.6}$$

and introduce the corresponding traditional imaging function as follows:

$$\mathfrak{F}_{\rm BFT}(\mathbf{r}) = |\mathbf{W}(\mathbf{r})\mathbb{M}\mathbf{W}(\mathbf{r})^T| = \left| \sum_{n=1}^{N} \sum_{m=1}^{M} \frac{S_{\rm scat}(n,m)}{\mathrm{E}^{(z)}_{\rm inc}(\mathbf{a}_m, \mathbf{r})\mathrm{E}^{(z)}_{\rm inc}(\mathbf{a}_n, \mathbf{r})} \right|.$$

A map of $f_{\rm BFT}(\mathbf{r})$ is expected to include peaks of large magnitude at $\mathbf{r} \in \Sigma$.

2.4. **Bifocusing Method Without Background Information.** It is essential to emphasize that unlike to traditional research, it is difficult to handle the diagonal elements of $\mathbb{M}$ because each N antenna is used to transmit signals and the remaining antennas are used to receive signals, referencing [36] as an example of this setup. Moreover, it is generally difficult to discern the weak scattered signal from the relatively high antenna reflection if the locations of antennas to transmit and receive signals are same, referencing [9]. Subsequently, we set unknown measurement data $S_{\rm scat}(n,n)$ to zero for all n and use the following scattering matrix:

$$\mathbb{D} = \begin{pmatrix} 0 & S_{\rm scat}(1,2) & \cdots & S_{\rm scat}(1,N-1) & S_{\rm scat}(1,N) \\ S_{\rm scat}(2,1) & 0 & \cdots & S_{\rm scat}(2,N-1) & S_{\rm scat}(2,N) \\ \vdots & \vdots & \ddots & \vdots & \vdots \\ S_{\rm scat}(N-1,1) & S_{\rm scat}(N-1,2) & \cdots & 0 & S_{\rm scat}(N-1,N) \\ S_{\rm scat}(N,1) & S_{\rm scat}(N,2) & \cdots & S_{\rm scat}(N,N-1) & 0 \end{pmatrix}. \tag{2.7}$$

We next generate the test vector (2.6) to be applied when the background information is unknown. Since the incident field $\mathrm{E}^{(z)}_{\rm inc}(\mathbf{r}, \mathbf{r}')$ is modeled by the following two-dimensional Greens' function:

$$\mathrm{E}^{(z)}_{\rm inc}(\mathbf{r}, \mathbf{r}') = \frac{i}{4} H_0^{(2)}(k|\mathbf{r} - \mathbf{r}'|) := G(\mathbf{r}, \mathbf{r}', k), \quad \mathbf{r} \neq \mathbf{r}',$$

the exact value of $\varepsilon_{\rm b}$ and $\sigma_{\rm b}$ must be known to produce exact incident field data. Here, $H_0^{(2)}$ denotes the Hankel function of order zero of the second kind. However, since we have no a priori information regarding $\varepsilon_{\rm b}$ and $\sigma_{\rm b}$, it is not possible to generate accurate incident field data (i.e., we cannot apply (2.6) to design the imaging function). Accordingly, we apply an alternative wavenumber η and generate the following test vector: for each $\mathbf{r} \in \Omega$,

$$\mathbf{G}(\mathbf{r}, \eta) = \left(\frac{1}{G(\mathbf{a}_1, \mathbf{r}, \eta)}, \frac{1}{G(\mathbf{a}_2, \mathbf{r}, \eta)}, \cdots, \frac{1}{G(\mathbf{a}_N, \mathbf{r}, \eta)} \right). \tag{2.8}$$

With this, we design the following imaging function for the BFM:

$$\mathfrak{F}_{\mathrm{BFM}}(\mathbf{r},\eta)=|\mathbf{G}(\mathbf{r},\eta)\mathbb{D}\mathbf{G}(\mathbf{r},\eta)^T|=\left|\sum_{n=1}^{N}\sum_{m=1}^{M}\frac{S_{\mathrm{scat}}(n,m)}{G(\mathbf{a}_m,\mathbf{r},\eta)G(\mathbf{a}_n,\mathbf{r},\eta)}\right|.$$

3. Theoretical Result

If the exact wavenumber k is applied, exact locations $\mathbf{r}_s\in\Sigma$ can be identified referencing the map of $\mathfrak{F}_{\mathrm{BFM}}(\mathbf{r},k)$; however, based on the simulation results exhibited in Section 4, inaccurate locations for $\mathbf{r}_s$ are retrieved when $\eta\neq k$. We next theoretically explain the reason for this phenomenon. To this end, we derive the following result.

Theorem 3.1. *Let* $\boldsymbol{\theta}_n=\mathbf{a}_n/|\mathbf{a}_n|=\mathbf{a}_n/R=(\cos\theta_n,\sin\theta_n)$ *and* $k\mathbf{r}'-\eta\mathbf{r}=|k\mathbf{r}'-\eta\mathbf{r}|(\cos\phi',\sin\phi')$. *If* $\mathbf{a}_n$ *satisfies* $|\mathbf{a}_n-\mathbf{r}'|\gg 1/4|k|,1/4|\eta|$ *for* $n=1,2,\cdots,N$, $\mathfrak{F}_{\mathrm{BFM}}(\mathbf{r})$ *can be represented as follows:*

$$\mathfrak{F}_{\mathrm{BFM}}(\mathbf{r},\eta)=\left|\frac{\eta}{4k\omega\mu_{\mathrm{b}}}\int_{\Sigma}\mathcal{O}(\mathbf{r}')\left[N^2\left(J_0(|k\mathbf{r}'-\eta\mathbf{r}|)+\frac{\Lambda(k,\eta)}{N}\right)^2\right.\right.$$
$$\left.\left.-N\left(J_0(2|k\mathbf{r}'-\eta\mathbf{r}|)+\frac{\Lambda(2k,2\eta)}{N}\right)\right]\mathrm{d}\mathbf{r}'\right|, \quad (3.1)$$

where J_p *denotes Bessel function of order* p *of the first kind and*

$$\Lambda(k,\eta)=\sum_{n=1}^{N}\sum_{p=-\infty,p\neq 0}^{\infty}i^pJ_p(|k\mathbf{r}'-\eta\mathbf{r}|)e^{ip(\theta_n-\phi')}.$$

Proof. Based on (2.4), (2.7), and (2.8), we can observe the following:

$$\begin{aligned}\mathbf{G}(\mathbf{r},\eta)\mathbb{D}\mathbf{G}(\mathbf{r},\eta)^T&=\sum_{n=1}^{N}\sum_{m=1}^{M}\frac{S_{\mathrm{scat}}(n,m)}{G(\mathbf{a}_m,\mathbf{r},\eta)G(\mathbf{a}_n,\mathbf{r},\eta)}\\&=\frac{i}{4\omega\mu_{\mathrm{b}}}\int_{\Sigma}\mathcal{O}(\mathbf{r}')\left[\left(\sum_{n=1}^{N}\frac{G(\mathbf{a}_n,\mathbf{r}',k)}{G(\mathbf{a}_n,\mathbf{r},\eta)}\right)^2-\sum_{n=1}^{N}\left(\frac{G(\mathbf{a}_n,\mathbf{r}',k)}{G(\mathbf{a}_n,\mathbf{r},\eta)}\right)^2\right]\mathrm{d}\mathbf{r}' \quad (3.2)\end{aligned}$$

Since $|\mathbf{a}_n-\mathbf{r}|,|\mathbf{a}_n-\mathbf{r}'|\gg 1/4|k|$ and $1/4|\eta|$ for all $n=1,2,\cdots,N$ and $s=1,2,\cdots,S$, the following asymptotic forms of the Hankel function holds (e.g., see [37, Theorem 2.5]):

$$H_0^{(2)}(k|\mathbf{a}_n-\mathbf{r}'|)\approx\frac{(1+i)e^{-ik|\mathbf{a}_n|}}{\sqrt{k\pi|\mathbf{a}_n|}}e^{ik\boldsymbol{\theta}_n\cdot\mathbf{r}'}\quad\text{and}\quad H_0^{(2)}(\eta|\mathbf{a}_n-\mathbf{r}|)\approx\frac{(1+i)e^{-i\eta|\mathbf{a}_n|}}{\sqrt{\eta\pi|\mathbf{a}_n|}}e^{i\eta\boldsymbol{\theta}_n\cdot\mathbf{r}}.$$

Thus, we have

$$\frac{G(\mathbf{a}_n,\mathbf{r}',k)}{G(\mathbf{a}_n,\mathbf{r},\eta)}=\frac{iH_0^{(2)}(k|\mathbf{a}_n-\mathbf{r}'|)/4}{iH_0^{(2)}(\eta|\mathbf{a}_n-\mathbf{r}|)/4}\approx\sqrt{\frac{\eta}{k}}e^{-i(k-\eta)|R|}e^{i\boldsymbol{\theta}_n\cdot(k\mathbf{r}'-\eta\mathbf{r})}.$$

Since $\boldsymbol{\theta}_n \cdot (k\mathbf{r}' - \eta\mathbf{r}) = |k\mathbf{r}' - \eta\mathbf{r}| \cos(\theta_n - \phi')$ and the following Jacobi-Anger expansion holds uniformly:

$$e^{ix\cos\theta} = J_0(x) + \sum_{p=-\infty, p\neq 0}^{\infty} i^p J_p(x) e^{ip\theta},$$

we can easily obtain

$$\sum_{n=1}^{N} \frac{G(\mathbf{a}_n, \mathbf{r}', k)}{G(\mathbf{a}_n, \mathbf{r}, \eta)} = \sqrt{\frac{\eta}{k}} e^{-i(k-\eta)|R|} \sum_{n=1}^{N} e^{i\boldsymbol{\theta}_n \cdot (k\mathbf{r}' - \eta\mathbf{r})} = \sqrt{\frac{\eta}{k}} \sum_{n=1}^{N} e^{i|k\mathbf{r}' - \eta\mathbf{r}| \cos(\theta_n - \phi')}$$
$$= N\sqrt{\frac{\eta}{k}} e^{-2i(k-\eta)|R|} \left(J_0(|k\mathbf{r}' - \eta\mathbf{r}|) + \frac{1}{N} \sum_{n=1}^{N} \sum_{p=-\infty, p\neq 0}^{\infty} i^p J_p(|k\mathbf{r}' - \eta\mathbf{r}|) e^{ip(\theta_n - \phi')} \right),$$

and similarly

$$\sum_{n=1}^{N} \left(\frac{G(\mathbf{a}_n, \mathbf{r}', k)}{G(\mathbf{a}_n, \mathbf{r}, \eta)} \right)^2 = \frac{\eta}{k} e^{-2i(k-\eta)|R|} \sum_{n=1}^{N} e^{2ik\boldsymbol{\theta}_n \cdot (\mathbf{r}' - \mathbf{r})}$$
$$= \frac{N\eta}{k} e^{-2i(k-\eta)|R|} \left(J_0(2|k\mathbf{r}' - \eta\mathbf{r}|) + \frac{1}{N} \sum_{n=1}^{N} \sum_{p=-\infty, p\neq 0}^{\infty} i^p J_p(2|k\mathbf{r}' - \eta\mathbf{r}|) e^{ip(\theta_n - \phi')} \right).$$

Therefore, we obtain the following:

$$\left(\sum_{n=1}^{N} \frac{G(\mathbf{a}_n, \mathbf{r}', k)}{G(\mathbf{a}_n, \mathbf{r}, \eta)} \right)^2 - \sum_{n=1}^{N} \left(\frac{G(\mathbf{a}_n, \mathbf{r}', k)}{G(\mathbf{a}_n, \mathbf{r}, \eta)} \right)^2 = \frac{N^2\eta}{k} e^{-i(k-\eta)|R|}$$
$$\times \left(J_0(|k\mathbf{r}' - \eta\mathbf{r}|) + \frac{\Lambda(k,\eta)}{N} \right)^2 - e^{-2i(k-\eta)|R|} \frac{N\eta}{k} \left(J_0(2|k\mathbf{r}' - \eta\mathbf{r}|) + \frac{\Lambda(2k, 2\eta)}{N} \right). \tag{3.3}$$

Since $|e^{-i(k-\eta)|R|}| = |e^{-2i(k-\eta)|R|}| = 1$, by combining (3.2) and (3.3), the structure (3.1) can be derived. □

Based on the Theorem 3.1, the map of $\mathfrak{F}_{\mathrm{BFM}}(\mathbf{r}, \eta)$ will contain peaks of large magnitudes at $\mathbf{r} = (k/\eta)\mathbf{r}'$ because $J_0(|k\mathbf{r}' - \eta\mathbf{r}|)$ reaches its maximum value when $|k\mathbf{r}' - \eta\mathbf{r}| = 0$. This is the theoretical reason why accurate locations and shapes of small anomalies cannot be retrieved using the map of $\mathfrak{F}_{\mathrm{BFM}}(\mathbf{r}, \eta)$ without background information (exact value of ε_{b} and σ_{b}). We will examine some further properties of $\mathfrak{F}_{\mathrm{BFM}}(\mathbf{r}, \eta)$ by applying a numerical simulation.

4. Simulation Results and Discussions

To support the result in Theorem 3.1, we present some numerical simulation results at angular frequency $\omega = 2\pi f$ with $f = 1\,\mathrm{GHz}$. To this end, we select two small anomalies Σ_s with radii $\alpha_s = 0.01\,\mathrm{m}$; locations $\mathbf{r}_1 = (0.01\,\mathrm{m}, 0.03\,\mathrm{m})$, and $\mathbf{r}_2 = (-0.04\,\mathrm{m}, -0.02\,\mathrm{m})$;

material properties $(\varepsilon_1, \sigma_1) = (55\varepsilon_0, 1.2\,\mathrm{S/m})$ and $(\varepsilon_2, \sigma_2) = (45\varepsilon_0, 1.0\,\mathrm{S/m})$; and $\varepsilon_0 = 8.854 \times 10^{-12}\,\mathrm{F/m}$ as the vacuum permittivity. We set the homogeneous background to be filled by a matching liquid with material properties $(\varepsilon_\mathrm{b}, \sigma_\mathrm{b}) = (20\varepsilon_0, 0.2\,\mathrm{S/m})$ and the imaging region Ω is $(-0.1\,\mathrm{m}, 0.1\,\mathrm{m}) \times (-0.1\,\mathrm{m}, 0.1\,\mathrm{m})$. To transmit and receive signals, we use $N = 16$ dipole antennas $\mathbf{A}_n$ with the following locations:

$$\mathbf{a}_n = 0.09\,\mathrm{m}(\cos\theta_n, \sin\theta_n), \quad \theta_n = \frac{2n\pi}{N}.$$

With this setting, the measurement data $S_\mathrm{scat}(n, m)$ and the incident field $G(\mathbf{a}_n, \mathbf{r}, \eta)$ for each $\mathbf{r} \in \Omega$ and η are generated by using CST STUDIO SUITE. After the generation of the measurement data, a $20\,\mathrm{dB}$ white Gaussian random noise was added. Figure 2 illustrates numerical simulation with and without anomalies.

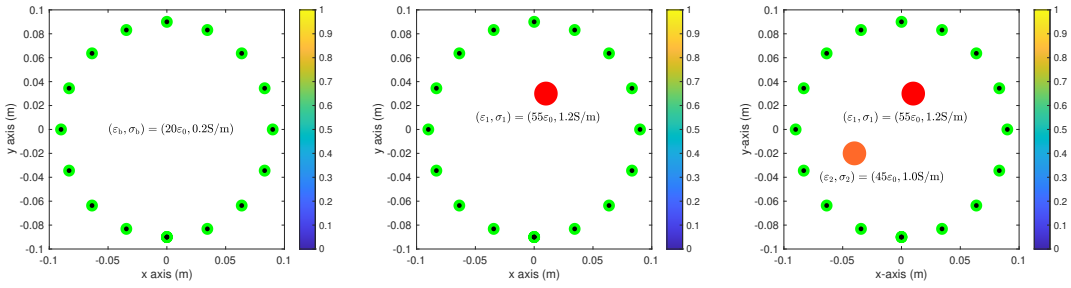

(a) Homogeneous Background (b) Single Anomaly (c) Multiple Anomalies

FIGURE 2. Illustration of the Numerical Simulations.

Example 4.1 (Inaccurate Background Permittivity). We first assume that only the exact value of ε_b is unknown i.e., we apply ε' instead of the true ε_b and corresponding wavenumber $\eta_\varepsilon = \omega\sqrt{\mu_\mathrm{b}(\varepsilon' + i\sigma_\mathrm{b}/\omega)}$. In this case, since $\omega\varepsilon_\mathrm{b} \gg \sigma_\mathrm{b}$, the identified location is as follows:

$$\mathbf{r} = \left(\frac{k}{\eta_\varepsilon}\right)\mathbf{r}' = \sqrt{\frac{\omega\varepsilon_\mathrm{b} + i\sigma_\mathrm{b}}{\omega\varepsilon' + i\sigma_\mathrm{b}}}\mathbf{r}' \approx \sqrt{\frac{\varepsilon_\mathrm{b}}{\varepsilon'}}\mathbf{r}'.$$

Hence, we can observe that if $\varepsilon' > \varepsilon_\mathrm{b}$, then the identified locations $(k/\eta_\varepsilon)\mathbf{r}'$ will be concentrated to the origin and the size of the identified anomaly will be smaller than the true anomaly. Otherwise, if $\varepsilon' < \varepsilon_\mathrm{b}$, then the identified locations $(k/\eta_\varepsilon)\mathbf{r}'$ will be situated far from the origin and the size of identified anomaly will be larger than the true anomaly. Figure 3 illustrates this outcome.

Figure 4 presents maps of $\mathfrak{F}_\mathrm{BFM}(\mathbf{r}, \eta_\varepsilon)$ with various selection of ε' for identifying a single anomaly Σ_1. Following the result of Theorem 3.1, an inaccurate locations $(k/\eta_\varepsilon)\mathbf{r}' \in \Sigma_1$ was identified instead of the true one $\mathbf{r}'$. Notice that the identified location and size of Σ_1 is close to the origin and smaller than the true one, respectively when $\varepsilon' > \varepsilon_\mathrm{b}$. In contrast, if $\varepsilon' < \varepsilon_\mathrm{b}$, the identified location and size of Σ_1 is far from the origin and larger than the true one, respectively.

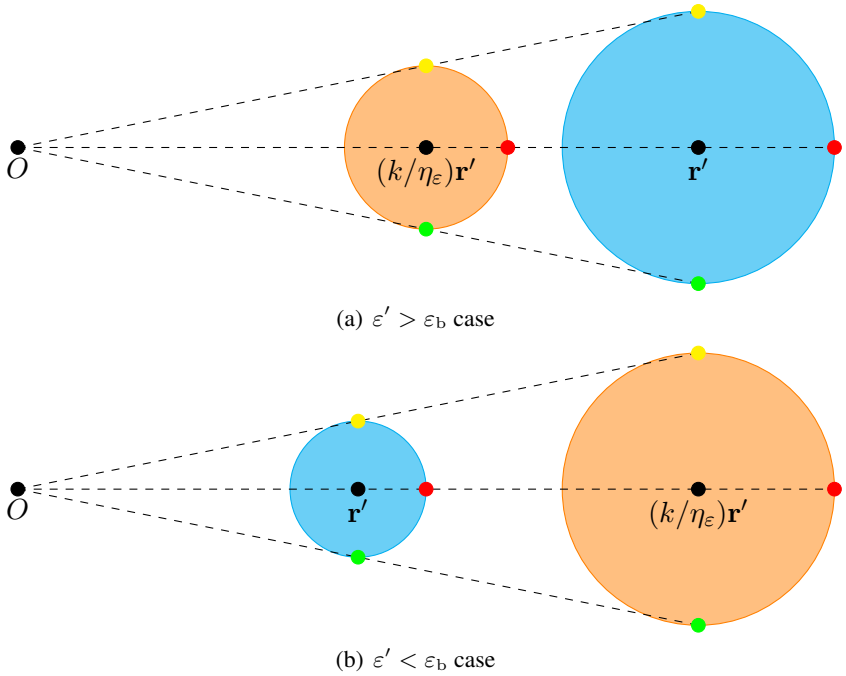

(a) $\varepsilon' > \varepsilon_{\mathrm{b}}$ case

(b) $\varepsilon' < \varepsilon_{\mathrm{b}}$ case

FIGURE 3. Description of the simulation result. Cyan- and orange-colored circles are true and identified anomalies via $\mathfrak{F}_{\mathrm{BFM}}(\mathbf{r}, \eta_\varepsilon)$, respectively.

Figure 5 exhibits maps of $\mathfrak{F}_{\mathrm{BFM}}(\mathbf{r}, \eta_\varepsilon)$ with various selection of ε' in the presence of Σ_1 and Σ_2. Similar to the results in Fig. 4, the identified locations $\mathbf{r}_s$ are concentrated when $\varepsilon' > \varepsilon_{\mathrm{b}}$ and scattered when $\varepsilon' < \varepsilon_{\mathrm{b}}$.

Finally, it is noteworthy that we are only able to recognize the existence of small anomalies from the map of $\mathfrak{F}_{\mathrm{BFM}}(\mathbf{r}, \eta_\varepsilon)$. Moreover, if $\varepsilon' \gg \varepsilon_{\mathrm{b}}$, it will be difficult to recognize small anomaly because several artifacts will be included in the map of $\mathfrak{F}_{\mathrm{BFM}}(\mathbf{r}, \eta_\varepsilon)$, and identified shape will be too small to distinguish from the artifacts (refer to Figs. 4(c) and 5(c)).

Example 4.2 (Inaccurate Background Conductivity). We next assume that only the exact value of σ_{b} is unknown i.e., we apply σ' instead of the true σ_{b} and corresponding wavenumber $\eta_\sigma = \omega\sqrt{\mu_{\mathrm{b}}(\varepsilon_{\mathrm{b}} + i\sigma'/\omega)}$. In this case, if $\omega\varepsilon_{\mathrm{b}} \gg \sigma_{\mathrm{b}}, \sigma'$, the identified location becomes

$$\mathbf{r} = \left(\frac{k}{\eta_\varepsilon}\right)\mathbf{r}' = \sqrt{\frac{\omega\varepsilon_{\mathrm{b}} + i\sigma_{\mathrm{b}}}{\omega\varepsilon_{\mathrm{b}} + i\sigma'}}\mathbf{r}' \approx \mathbf{r}'.$$

Hence, in contrast to Example 4.1, it will be possible to identify the almost true location and shape of Σ_s by selecting a small value of σ'.

Figure 6 shows maps of $\mathfrak{F}_{\mathrm{BFM}}(\mathbf{r}, \eta_\sigma)$ with various selection of σ' for identifying single anomaly Σ_1. Following the result in Theorem 3.1, the locations $(k/\eta_\sigma)\mathbf{r}'$ for $\mathbf{r}' \in \Sigma_1$ is

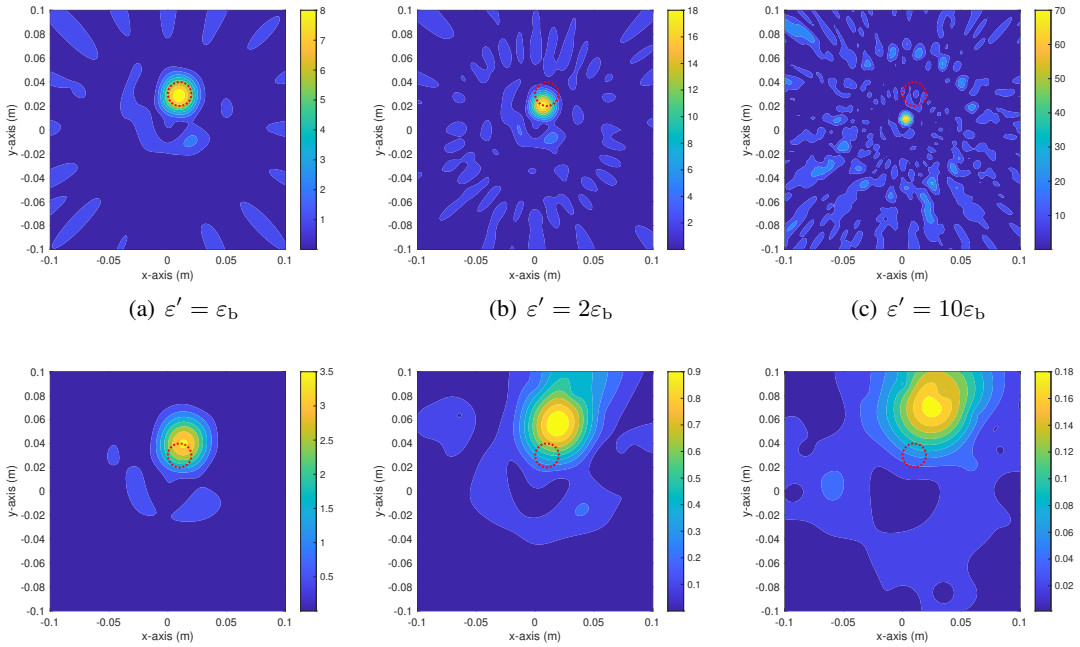

(a) $\varepsilon' = \varepsilon_{\mathrm{b}}$ (b) $\varepsilon' = 2\varepsilon_{\mathrm{b}}$ (c) $\varepsilon' = 10\varepsilon_{\mathrm{b}}$

(d) $\varepsilon' = 0.5\varepsilon_{\mathrm{b}}$ (e) $\varepsilon' = 0.2\varepsilon_{\mathrm{b}}$ (f) $\varepsilon' = 0.01\varepsilon_{\mathrm{b}}$

FIGURE 4. (Example 4.1) Maps of $\mathfrak{F}_{\mathrm{BFM}}(\mathbf{r}, \eta_\varepsilon)$ with various selection of ε'. Red-colored dashed circles are the boundaries of anomalies.

identified; however, when the selected value of σ' is small or satisfies $\omega\varepsilon_{\mathrm{b}} \gg \sigma'$, the almost true location and size of Σ_1 is retrieved because $(k/\eta_\varepsilon)\mathbf{r}' \approx \mathbf{r}' \in \Sigma_1$. However, if condition $\omega\varepsilon_{\mathrm{b}} \gg \sigma'$ does not hold, it is not possible to identify the location $\mathbf{r}' \in \Sigma_1$. Moreover, in contrast to the results in Example 4.1, the existence of anomalies cannot be recognized via the map of $\mathfrak{F}_{\mathrm{BFM}}(\mathbf{r}, \eta_\sigma)$.

Figure 7 exhibits maps of $\mathfrak{F}_{\mathrm{BFM}}(\mathbf{r}, \eta_\sigma)$ with various selection of σ' in the presence of Σ_1 and Σ_2. Similar to the results in Fig. 6, although some artifacts are included in the map, it is possible to identify the almost true location and size of anomalies if $\omega\varepsilon_{\mathrm{b}} \gg \sigma'$ or σ' is very small; however, it is not possible to recognize the existence of anomalies if condition $\omega\varepsilon_{\mathrm{b}} \gg \sigma'$ does not hold.

5. CONCLUSION

Based on the integral equation for the scattered-field $S-$parameter in the presence of small anomalies, the mathematical structure of the imaging function of the BFM was investigated by establishing a relationship with an infinite series of Bessel functions, antenna arrangements, and anomaly properties when the exact values of background permittivity and conductivity are

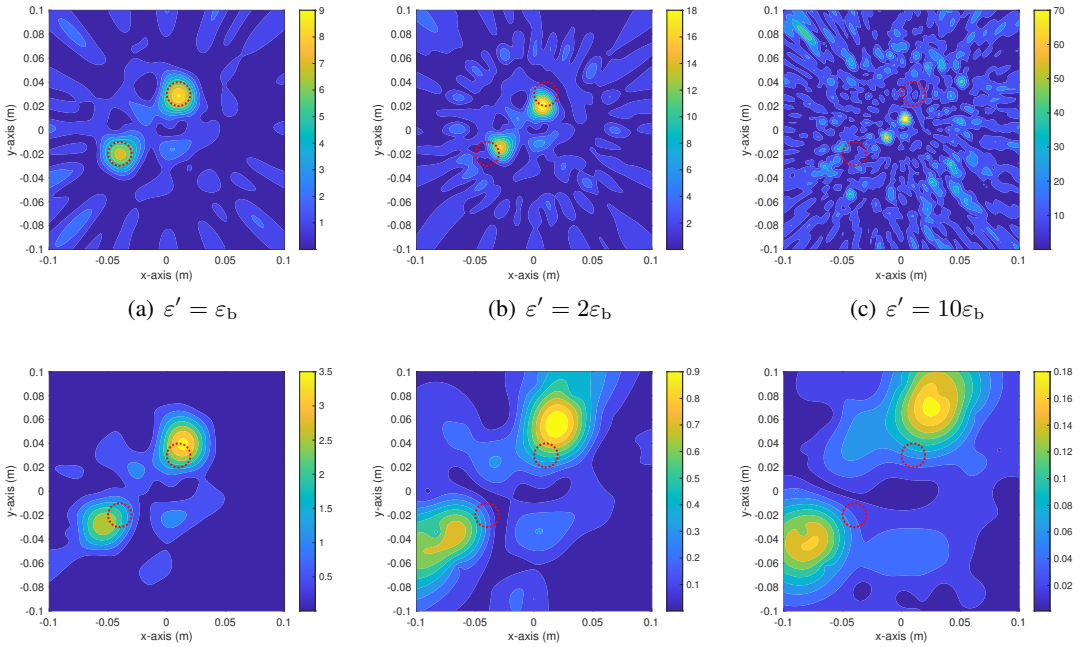

(a) $\varepsilon' = \varepsilon_{\mathrm{b}}$ (b) $\varepsilon' = 2\varepsilon_{\mathrm{b}}$ (c) $\varepsilon' = 10\varepsilon_{\mathrm{b}}$

(d) $\varepsilon' = 0.5\varepsilon_{\mathrm{b}}$ (e) $\varepsilon' = 0.2\varepsilon_{\mathrm{b}}$ (f) $\varepsilon' = 0.01\varepsilon_{\mathrm{b}}$

FIGURE 5. (Example 4.1) Maps of $\mathfrak{F}_{\mathrm{BFM}}(\mathbf{r}, \eta_\varepsilon)$ with various selection of ε'. Red-colored dashed circles are the boundaries of anomalies.

unknown. Based on the structure investigated, we confirmed the reason that the locations of anomalies were identified inaccurately. Based on the simulation results using noisy data, we determined that the identified location and size of anomalies are inaccurate when inaccurate values for background permittivity were applied, but almost true location and size of anomalies are retrieved when the inaccurate value of background conductivity is very small.

In this study, we considered the imaging of small, circle-like, two-dimensional anomalies. Extension to arbitrarily shaped large anomalies in two- and three- dimensional problems will be an interesting and significant research subject. Moreover, we performed the simulation using synthetic data, conducting mathematical analyses and numerical simulations using real-world microwave imaging. Development and investigation of an effective algorithm for estimating background wavenumbers will be the subject of forthcoming work.

ACKNOWLEDGMENTS

This research was supported by the Soonchunhyang University Research Fund and the National Research Foundation of Korea (NRF) grant funded by the Korea government (MSIT) (NRF-2020R1A2C1A01005221).

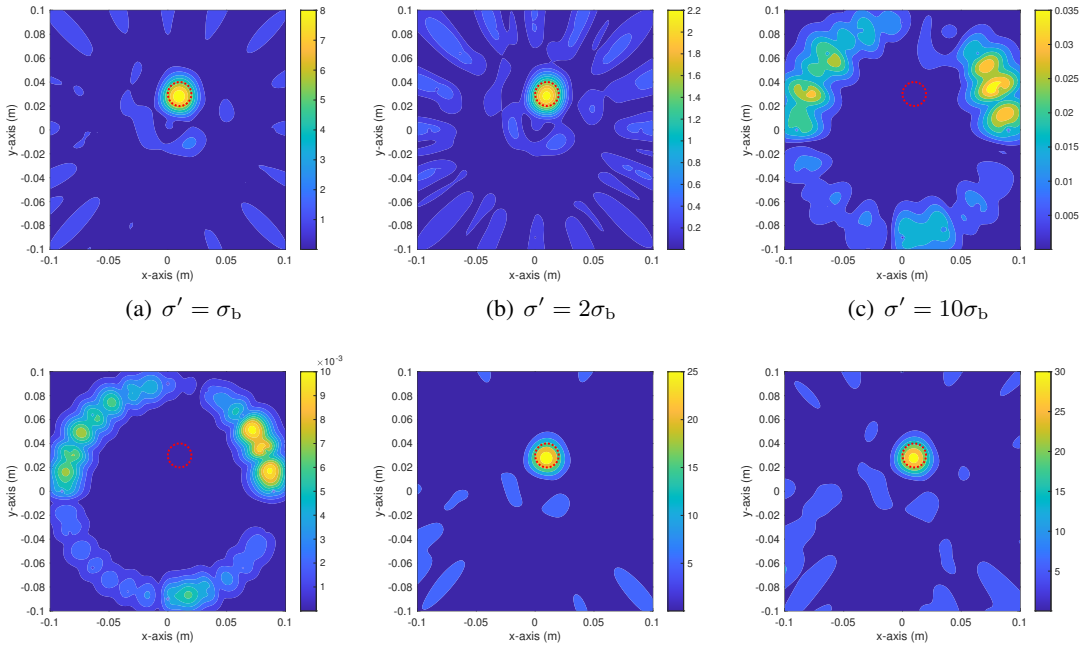

(a) $\sigma' = \sigma_{\mathrm{b}}$ (b) $\sigma' = 2\sigma_{\mathrm{b}}$ (c) $\sigma' = 10\sigma_{\mathrm{b}}$

(d) $\sigma' = 20\sigma_{\mathrm{b}}$ (e) $\sigma' = 0.2\sigma_{\mathrm{b}}$ (f) $\sigma' = 0.01\sigma_{\mathrm{b}}$

FIGURE 6. (Example 4.2) Maps of $\mathfrak{F}_{\mathrm{BFM}}(\mathbf{r}, \eta_\sigma)$ with various selection of σ'. Red-colored dashed circles are the boundaries of anomalies.

REFERENCES

[1] K. Ito, B. Jin, and J. Zou, *A direct sampling method to an inverse medium scattering problem*, Inverse Problems, **28** (2012), Article No. 025003.

[2] S. Kang, M. Lambert, and W.-K. Park, *Direct sampling method for imaging small dielectric inhomogeneities: analysis and improvement*, Inverse Problems, **34** (2018), Article No. 095005.

[3] S.-H. Son, K.-J. Lee, and W.-K. Park, *Application and analysis of direct sampling method in real-world microwave imaging*, Applied Mathematics Letters, **96** (2019), 47–53.

[4] S. Coşğun, E. Bilgin, and M. Çayören, *Microwave imaging of breast cancer with factorization method: SPIONs as contrast agent*, Medical Physics, **47** (2020), 3113–3122.

[5] J. Guo, G. Yan, J. Jin, and J. Hu, *The factorization method for cracks in inhomogeneous media*, Applications of Mathematics, **62** (2017), 509–533.

[6] K. H. Leem, J. Liu, and G. Pelekanos, *An extended direct factorization method for inverse scattering with limited aperture data*, Inverse Problems in Science and Engineering, **28** (2020), 754–776.

[7] H. Ammari, J. Garnier, H. Kang, W.-K. Park, and K. Sølna, *Imaging schemes for perfectly conducting cracks*, SIAM Journal on Applied Mathematics, **71** (2011), 68–91.

[8] H. Ammari, J. Garnier, H. Kang, M. Lim, and K. Sølna, *Multistatic imaging of extended targets*, SIAM Journal on Imaging Sciences, **5** (2012), 564–600.

[9] W.-K. Park, *Real-time microwave imaging of unknown anomalies via scattering matrix*, Mechanical Systems and Signal Processing, **118** (2019), 658–674.

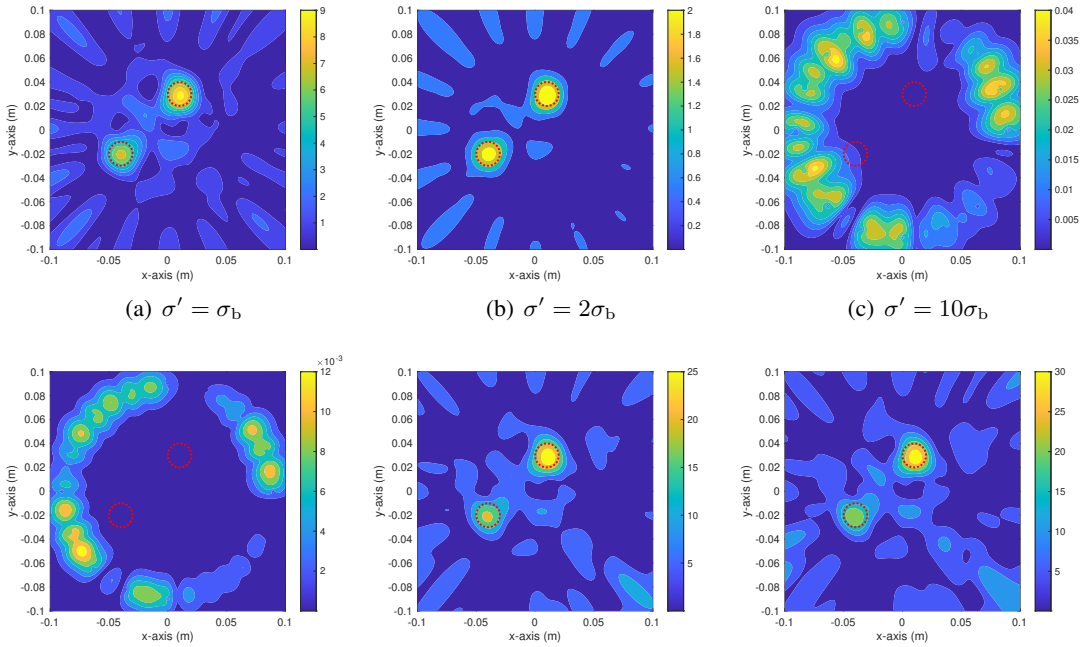

(a) $\sigma' = \sigma_{\mathrm{b}}$ (b) $\sigma' = 2\sigma_{\mathrm{b}}$ (c) $\sigma' = 10\sigma_{\mathrm{b}}$

(d) $\sigma' = 20\sigma_{\mathrm{b}}$ (e) $\sigma' = 0.2\sigma_{\mathrm{b}}$ (f) $\sigma' = 0.01\sigma_{\mathrm{b}}$

FIGURE 7. (Example 4.2) Maps of $\mathfrak{F}_{\mathrm{BFM}}(\mathbf{r}, \eta_\sigma)$ with various selection of σ'. Red-colored dashed circles are the boundaries of anomalies.

[10] H. F Alqadah, *A compressive multi-frequency linear sampling method for underwater acoustic imaging*, IEEE Transactions on Image Processing, **25** (2016), 2444–2455.

[11] L. Audibert and H. Haddar, *The generalized linear sampling method for limited aperture measurements*, SIAM Journal on Imaging Sciences, **10** (2017), 845–870.

[12] M. G. Aram, M. Haghparast, M. S. Abrishamian, and A. Mirtaheri, *Comparison of imaging quality between linear sampling method and time reversal in microwave imaging problems*, Inverse Problems in Science and Engineering, **24** (2016), 1347–1363.

[13] Q. Bao, S. Yuan, and F. Guo, *A new synthesis aperture-MUSIC algorithm for damage diagnosis on complex aircraft structures*, Mechanical Systems and Signal Processing, **136** (2010), Article No. 106491.

[14] W.-K. Park, *Asymptotic properties of MUSIC-type imaging in two-dimensional inverse scattering from thin electromagnetic inclusions*, SIAM Journal on Applied Mathematics, **75** (2015), 209–228.

[15] W.-K. Park, *Application of MUSIC algorithm in real-world microwave imaging of unknown anomalies from scattering matrix*, Mechanical Systems and Signal Processing, **153** (2021), Article No. 107501.

[16] M. N. Akinci, M. Çayören, and İ. Akduman, *Near-field orthogonality sampling method for microwave imaging: theory and experimental verification*, IEEE Transactions on Microwave Theory and Techniques, **64** (2016), 2489–2501.

[17] M. T. Bevacqua, T. Isernia, R. Palmeri, M. N. Akinci, and L. Crocco, *Physical insight unveils new imaging capabilities of orthogonality sampling method*, IEEE Transactions on Antennas and Propagation, **68** (2020), 4014–4021.

[18] W.-K. Park, *On the application of orthogonality sampling method for object detection in microwave imaging*, IEEE Transactions on Antennas and Propagation, **71** (2023), 934–946.
[19] M. Bonnet, *Fast identification of cracks using higher-order topological sensitivity for 2-D potential problems*, Engineering Analysis with Boundary Elements, **35** (2011), 223–235.
[20] F. Le Louër and M.-L. Rapún, *Topological sensitivity for solving inverse multiple scattering problems in 3D electromagnetism. Part I: one step method*, SIAM Journal on Imaging Sciences, **10** (2017), 1291–1321.
[21] W.-K. Park, *Performance analysis of multi-frequency topological derivative for reconstructing perfectly conducting cracks*, Journal of Computational Physics, **335** (2017), 865–884.
[22] H. Ammari, J. Garnier, W. Jing, H. Kang, M. Lim, K. Sølna, and H. Wang, *Mathematical and statistical methods for multistatic imaging*,Lecture Notes in Mathematics 2098, Springer, Cham, 2013.
[23] H. Ammari and H. Kang, *Reconstruction of Small Inhomogeneities from Boundary Measurements*, Lecture Notes in Mathematics 1846, Springer-Verlag, Berlin, 2004.
[24] N. Bleistein, J. Cohen, and J. S. Stockwell Jr, *Mathematics of Multidimensional Seismic Imaging, Migration, and Inversion*, Interdisciplinary Applied Mathematics 13, Springer, New York, 2001.
[25] V. S. Chernyak, *Fundamentals of Multisite Radar Systems: Multistatic Radars and Multiradar Systems*, CRC Press, Routledge, 1998.
[26] F. Cakoni, D. Colton, and P. Monk, *The Linear Sampling Method in Inverse Electromagnetic Scattering*,CBMS-NSF Regional Conference Series in Applied Mathematics 80, Society for Industrial and Applied Mathematics, 2011.
[27] A. Kirsch and N. Grinberg, *The Factorization Method for Inverse Problems*, Oxford University Press, 2008.
[28] A. A. Novotny and J. Sokolowski, *Topological derivatives in shape optimization*, Interaction of Mechanics and Mathematics Series, Springer-Verlag, Berlin, Heidelberg, 2013.
[29] L. Jofre, A. Broquetas, J. Romeu, S. Blanch, A. P. Toda, X. Fabregas, and A. Cardama, *UWB tomographic radar imaging of penetrable and impenetrable objects*, Proceedings of the IEEE, **97** (2009), 451–464.
[30] Y. J. Kim, L. Jofre, F. De Flaviis, and M. Q. Feng, *Microwave reflection tomographic array for damage detection of civil structures*, IEEE Transactions on Antennas and Propagation, **51** (2003), 3022–3032.
[31] S. Kang, W.-K. Park, and S.-H. Son, *A qualitative analysis of the bifocusing method for a real-time anomaly detection in microwave imaging*, Computers and Mathematics with Applications, **137** (2023), 93–101.
[32] M. Slaney, A. C. Kak, and L. E. Larsen, *Limitations of imaging with first-order diffraction tomography*, IEEE Transactions on Microwave Theory and Techniques, **32** (1984), 860–874.
[33] W.-K. Park, H. P. Kim, K.-J. Lee, and S.-H. Son, *MUSIC algorithm for location searching of dielectric anomalies from $S-$parameters using microwave imaging*, Journal of Computational Physics, **348** (2017), 259–270.
[34] M. Haynes, J. Stang, and M. Moghaddam, *Real-time microwave imaging of differential temperature for thermal therapy monitoring*, IEEE Transactions on Biomedical Engineering, **61** (2014), 1787–1797.
[35] J.-Y. Kim, K.-J. Lee, B.-R. Kim, S.-I. Jeon, and S.-H. Son, *Numerical and experimental assessments of focused microwave thermotherapy system at* 925 MHz, ETRI Journal, **41** (2019), 850–862.
[36] S.-H. Son, N. Simonov, H.-J. Kim, J.-M. Lee, and S.-I. Jeon, *Preclinical prototype development of a microwave tomography system for breast cancer detection*, ETRI Journal, **32** (2010), 901–910.
[37] D. Colton and R. Kress, *Inverse Acoustic and Electromagnetic Scattering Problems*, Mathematics and Applications Series 93, Springer, New York, 1998.